

Engineering Notes

A Study of the Wind Sensing Performance of Small Pusher and Puller Hexacopters

Javier González-Rocha*

University of California, Santa Cruz, Santa Cruz,

California, 95064

Prashin Sharma[†]

University of Michigan, Ann Arbor, Michigan 48109 and

Ella Atkins[‡] and Craig Woolsey[§] Virginia Polytechnic Institute and State University,

Blacksburg, Virginia 24061

https://doi.org/10.2514/1.C036792

I. Introduction

ULTIROTOR small unmanned aircraft systems (SUASs) can increase the spatiotemporal resolution of wind observations near the Earth's surface [1-4]. Compared to mast towers, weather balloon radiosondes, and remote sensing wind profilers, multirotor SUASs are mobile, portable, low cost, and easy to maneuver in complex environments [5]. These characteristics of multirotor SUAS can revolutionize existing atmospheric sensor networks and give way to transformative advances for aviation and weather forecasting enterprises [6-9]. For instance, wind observations collected with multirotor SUASs can help map wind velocity fields in urban landscapes, which is critical for developing disturbance rejection and path planning algorithms for safe and efficient urban air mobility. Multirotor SUAS wind observations can also improve numerical weather prediction models: an imperative for increasing the accuracy of hyperlocal weather forecasts [4]. Therefore, developing reliable wind sensing techniques is important for realizing the full potential of multirotor SUASs for increasing velocity observations in the lower atmosphere.

Several studies have explored the use of multirotor SUASs and onboard low-cost sensors for atmospheric wind sensing. For example, multirotor SUAS atmospheric observations have been used to study the evolution of the atmospheric parameters [3,10,11], atmospheric transport of pollutants and biohazards [10,12], and source emissions of greenhouse gases [13,14]. Although wind observations from multirotor SUAS integrated sensors have been found to be reliable in stationary flight, exhaustive experiments are required to characterize systematic measurement biases resulting from vehicle

motion and propeller downwash effects. Moreover, the added weight and power requirements of airflow sensors also reduce the payload capacity and endurance of multirotor SUASs. Therefore, sensor-free alternatives for sensing wind velocity will become more relevant as multirotor SUASs continue to decrease in size.

A number of model-based methods have already been developed to estimate wind velocity from wind-induced motion perturbations instead of an airflow sensor [2,15]. A study comparing the performance of kinematic particle, point mass, and rigid-body models has found that the bandwidth and accuracy of model-based wind estimates improve with the fidelity of the vehicle motion models [2]. An extension of the rigid-body model wind estimation framework has also shown good efficiency in resolving vertical wind profiles ascending at steady rates of up to 2 m/s based on a comparison of wind observations from a sonic detection and ranging wind profiler [16]. These wind sensing algorithms have also been applied to study the drift of small objects, wind flow variations, and transport of aerosolized toxins in aquatic environments [5,17]. However, it remains unknown how the performance of model-based wind estimation varies across multirotor SUAS configurations.

A recent study examining the thrust generation of puller and pusher multirotors has shown the latter to have a lower lift-to-drag ratio in forward flight [18]. Differences in the lift-to-drag ratios of puller and pusher hexacopters are attributed to their respective propeller and airframe configurations. Puller hexacopters, which are more common, have the rotors installed above the rotor arms such that the multirotor airframe is pulled as thrust is generated. Pusher hexacopters have the rotors installed below the rotor arms such that the multirotor airframe is pushed as thrust is generated. The differences observed across puller and pusher multirotor SUASs may also provide opportunities for understanding how the fidelity of time-varying wind estimates compares across platforms with distinct lift-to-drag ratios.

This Note extends the model-based wind estimation algorithm presented in Ref. [2] to evaluate the performance of pusher and puller hexacopters estimating time-varying wind fluctuations. First, the closed-loop rigid-body dynamics of pusher and puller hexacopters were characterized using stepwise regression and output error algorithms for model structure determination and parameter estimation. The vehicle motion models identified for each aircraft were then used to synthesize state observers for wind estimation. Wind velocity estimates from state observers designed for pusher and puller hexacopter platforms were validated using wind velocity observations interpolated at the center of four sonic anemometers arranged in a tetrahedron configuration. To the best of the authors' knowledge, this research presents the first comprehensive study of the model-based wind estimation performance of pusher and puller hexacopter multirotors.

II. Modeling

The equations of motion for a feedback-stabilized hexacopter can be expressed as a system of first-order nonlinear time-invariant ordinary differential equations [2]:

$$\dot{x} = f(x, u, w(t, x)), \qquad x(t_0) = x_0$$
 (1)

where the rate of change \dot{x} of the vehicle's 12-dimensional state x (i.e., position, attitude, velocity, and angular velocity) relates to the state itself, the control inputs u, and translational wind disturbances w(t,x) varying over time and space. Moreover, when the aircraft motion is modeled as a small perturbation from some equilibrium flight condition that corresponds to hovering (i.e., $\dot{v} \equiv 0$ and $\dot{\omega} \equiv 0$), the nonlinear dynamics describing the feedback-stabilized motion of the hexacopter are well approximated by a linear model of the form

Received 15 December 2021; revision received 7 October 2022; accepted for publication 18 June 2023; published online 27 July 2023. Copyright © 2023 by the American Institute of Aeronautics and Astronautics, Inc. All rights reserved. All requests for copying and permission to reprint should be submitted to CCC at www.copyright.com; employ the eISSN 1533-3868 to initiate your request. See also AIAA Rights and Permissions www.aiaa.org/randp.

^{*}Assistant Professor, Department of Applied Mathematics. Member AIAA.

[†]Graduate Student, Robotics Institute. Student Member AIAA.

[‡]Professor and Department Head, Kevin T. Crofton Department of Aerospace Engineering, Fellow AIAA.

[§]Professor, Kevin T. Crofton Department of Aerospace and Ocean Engineering. Member AIAA.

$$\frac{d}{dt}\tilde{x} = A\tilde{x} + B\tilde{u} + \Gamma w \tag{2}$$

where the vectors of $\tilde{x} = x - x_{\rm eq}$ and $\tilde{u} = u - u_{\rm eq}$ denote, respectively, small deviations in the state and input vectors from their steady-state values. The state matrix $A \in \mathbb{R}^{12 \times 12}$ models unforced dynamics, the input matrix $B \in \mathbb{R}^{12 \times 4}$ characterizes applied forcing, and the disturbance matrix $\Gamma \in \mathbb{R}^{12 \times 3}$ captures wind-induced translational perturbations. Effects due to spatial wind gradients such as effective angular damping are ignored. We use this model form to estimate wind velocity while hovering in equilibrium flight using a state observer. The state observer is constructed based on the state, input, and disturbance matrices characterized from system identification experiments.

III. Multirotor System Identification

A. System Identification Overview

A number of frequency- and time-domain system identification algorithms have been developed to characterize bare-airframe and closed-loop dynamic models for multirotor aircraft. Frequency-domain system identification techniques have been used to characterize bare-airframe models using flight-test data collected from feedback-stabilized systems [19–22]. Reliable bare-airframe models are critical for validating physics-based simulations and control system designs. Time-domain system identification methods, such as the stepwise regression and output error algorithms described by Klein and Morelli (Ref. [23]), have been effective for characterizing multirotor aircraft closed-loop models; and they have already been used to estimate wind velocity from quadrotor motion in previous studies [1,2,16]. For this reason, time-domain system identification techniques were employed to characterize the closed-loop dynamics of puller and pusher aircraft.

B. System Identification Flight Testing

System identification experiments were conducted at the University of Michigan M-Air facility to characterize a set of linear time-invariant closed-loop models approximating the rigid dynamics of the pusher and puller hexacopter platforms described in Ref. [18]. Autonomous flights were conducted in calm atmospheric conditions (i.e., $V_{\rm w} \approx 0$ m/s) using a Qualisys motion capture system, which can measure position and orientation at 200 Hz. During each flight, the vehicle's plunge, yaw, roll, and pitch dynamics were excited from equilibrium flight separately using the frequency-sweep inputs:

$$u(i) = \sin[\phi(i)], \qquad i = 0, 1, 2, \dots, N - 1$$

$$\phi(i) = \omega(i)t(i)$$

$$\omega(i) = 10^{p}$$

$$p = \log_{10}\omega_0 + (\log_{10}\omega_1 - \log_{10}\omega_0)\frac{t(i)}{T}$$

where u is the commanded translational velocity, $\omega_0 = 0.5$ Hz, $\omega_1 = 4$ Hz, $T = (N-1)\Delta t$, and $t(i) = i\Delta t$. The maximum excitation frequency was determined based on sampling volume constraints. The input and output measurements collected from the flight controller and the motion capture system were then used to characterize the model structures and parameter estimates for the plunge, yaw, roll, and pitch dynamics separately by employing stepwise regression and output error parameter estimation algorithms.

C. Model Structure Determination

The stepwise regression algorithm described in Ref. [23] was employed to determine the parameter structure of linear time-invariant models approximating the plunge, yaw, roll, and pitch dynamics of each hexacopter in equilibrium flight. Using this approach, the vehicle state and input measurements are postulated as explanatory functions ξ_i , i = 1, 2, ..., n, to construct a model that best fits the vehicle's modeled response y, which is assumed to take the form

$$y = \theta_0 + \sum_{i=1}^n \theta_i \xi_i \tag{3}$$

where θ_i , $i=1,2,\ldots,n$, is the set of model coefficients associated with n regressor functions; θ_0 is the model bias; and N is the sample size of measurements. How well each model structure fits the observed data is determined using the F_0 statistic and coefficient of determination R^2 metrics because explanatory variables are considered for integration into the model one at a time. The F_0 statistic gives a measure of how much each explanatory variable contributes to the fit of the model. The coefficient of determination quantifies how well the output matches the measured data. Leveraging the two metrics together, model structures were determined for linear approximations of each hexacopter's plunge, yaw, roll, and pitch dynamics in equilibrium flight.

D. Parameter Estimation

The model structures and parameter values determined from the stepwise regression were used to initialize the estimation of model parameters using the output error algorithm described in Ref. [23]. The output error algorithm estimates model parameters using the output of the linear aircraft model described by Eq. (2) in still air conditions and using the N sample points of measured flight data, which are assumed to be corrupted by sensor noise ν . The model and measurements used by the output error method are summarized as follows:

$$\frac{d}{dt}\tilde{\mathbf{x}} = \mathbf{A}\tilde{\mathbf{x}} + \mathbf{B}\tilde{\mathbf{u}}, \qquad \tilde{\mathbf{x}}(0) = \mathbf{x}_0 \tag{4}$$

$$y = C\tilde{x} + D\tilde{u} \tag{5}$$

$$z(i) = y(i) + \nu(i)$$
 $i = 1, 2, ..., N$ (6)

where y is the output vector, z is the measurement vector, C is the output matrix, and D is the feedthrough matrix. This formulation of the output error method assumes that the model being identified is free of process noise, making numerical integration of state outputs possible. Moreover, we assume the flight measurements to be corrupted with uncorrelated zero-mean Gaussian noise $v \in \mathcal{N}(0, R_{\text{Cov}})$ such that

$$Cov(\nu(i)) = E[\nu(i)\nu^{T}(i)] = \mathbf{R}_{Cov}\delta_{ii}$$

Using this framework, parameter estimates are tuned iteratively while minimizing the cost function:

$$J = \frac{1}{2} \sum_{i=1}^{N} [\mathbf{y}(i) - \mathbf{z}(i)]^{T} \mathbf{R}_{Cov}^{-1} [\mathbf{y}(i) - \mathbf{z}(i)]$$
 (7)

which is the uncertainty-weighted residual between the model output and observation measurements.

IV. Observer Synthesis

The wind sensing method presented in Ref. [2] was adapted to synthesize observers used in estimating the hexacopter wind velocity. We assume that absolute measurements of the position and attitude and their respective time derivatives can be obtained from the motion capture system, Therefore, the output equation, as in Ref. [2], is of the form

$$y = \mathbb{I}_{12} ilde{x} + egin{pmatrix} \mathbf{0}_3 \ \mathbf{0}_3 \ \mathbb{I}_3 \ \mathbf{0}_3 \end{pmatrix} V_{\mathrm{w}}$$

where the output measurements of translational velocity are the summation of both air-relative and wind velocities (with the identity and zero

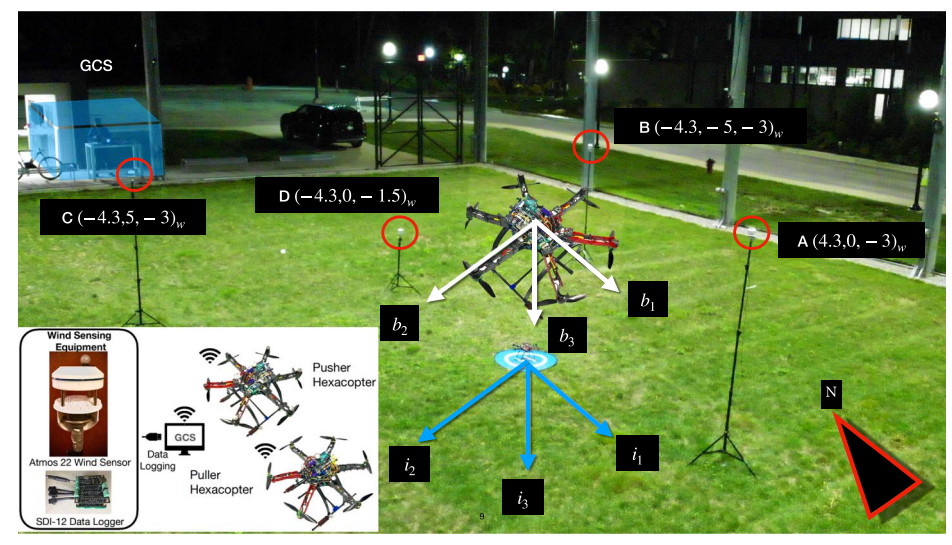


Fig. 1 Placement of wind sensors and hexacopter hover position for outdoor wind sensing experiments. All coordinates are in meters with respect to the inertial (ground) frame (shown in blue).

matrices written in short notation, e.g., $\mathbb{I}_{12} \in \mathbb{R}^{12 \times 12}$). Noise in the output measurement is assumed to be negligible, and it is therefore not modeled. The output measurements and identified models were then used to formulate wind-augmented models for the operating condition prescribed by v_{eq} .

V. Wind Sensing Experiments

A. Flight Testing

The outdoor experimental setup to collect the wind data and hexacopter response is shown in Fig. 1. These experiments were conducted in the M-Air [24] facility, where system identification experiments took place as well. This facility has motion capture (mocap) cameras that allow tracking of reflective markers fixed to the hexacopter, enabling accurate position tracking. The reflective targets were placed on the arms and the landing gear of the hexacopters such that the mocap virtual body centroid is as close as possible to the center of gravity of the hexacopter. Before flying, each hexacopter was placed at the center of the triangle represented by the (i_1, i_2, i_3) North-East-Down (NED) frame as shown in Fig. 1. The mocap had millimeter accuracy in position. The aircraft orientation was provided by the attitude and heading reference system that is integral to the onboard flight controller. A reference flight trajectory was created, enabling the hexacopter to autonomously take off and ascend to a height of 3 m, hover for 3 min, and land. Additionally, the hexacopters were also connected to the same ground control station (GCS) through Wi-Fi, as shown in Fig. 1. The data for the hexacopter system response (e.g., roll, pitch, yaw angular rates, and control commands) were collected on board at 200 Hz. To ensure the data from wind sensors and the hexacopter can be correlated, computer clock times between the hexacopter and the GCS were synchronized just before flight.

B. Atmospheric Sensors

To collect wind data for outdoor experiments, we used four Atmos 22 sonic anemometers. The anemometers were mounted on tripod stands as shown in Fig. 1 to form a tetrahedron, with all facing north. A reflective marker was placed on each sonic anemometer to record its absolute position. The placement of the anemometers was chosen to avoid collecting wind data from flow disturbed by the hexacopter and capture the ambient wind conditions only. The sonic anemometers were interfaced to the GCS computer through the SDI-12 universal

Table 1 Plunge, yaw, roll, and pitch model structures identified using stepwise regression

| Vehicle motion models | Formulas |
|-----------------------|--|
| Plunge | $\begin{pmatrix} \dot{z} \\ \dot{w} \end{pmatrix} = \begin{pmatrix} 0 & 1 \\ Z_z & Z_w \end{pmatrix} \begin{pmatrix} z \\ w \end{pmatrix} + \begin{pmatrix} 0 \\ Z_\mu \end{pmatrix} \mu_{\text{plunge}}$ |
| Yaw | $\begin{pmatrix} \dot{\psi} \\ \dot{r} \end{pmatrix} = \begin{pmatrix} 0 & 1 \\ N_{\psi} & N_{r} \end{pmatrix} \begin{pmatrix} \psi \\ r \end{pmatrix} + \begin{pmatrix} 0 \\ N_{\mu} \end{pmatrix} \mu_{\text{yaw}}$ |
| Roll | $ \begin{pmatrix} \dot{y} \\ \dot{\phi} \\ \dot{v} \\ \dot{p} \end{pmatrix} = \begin{pmatrix} 0 & 0 & 1 & 0 \\ 0 & 0 & 0 & 1 \\ 0 & Y_{\phi} & Y_{v} & Y_{p} \\ 0 & L_{\phi} & 0 & L_{p} \end{pmatrix} \begin{pmatrix} y \\ \phi \\ v \\ p \end{pmatrix} + \begin{pmatrix} 0 \\ 0 \\ 0 \\ L_{\mu} \end{pmatrix} \mu_{\text{roll}} $ |
| Pitch | $ \begin{pmatrix} \dot{x} \\ \dot{\theta} \\ \dot{u} \\ \dot{q} \end{pmatrix} = \begin{pmatrix} 0 & 0 & 1 & 0 \\ 0 & 0 & 0 & 1 \\ 0 & X_{\theta} & X_{u} & X_{q} \\ 0 & M_{\theta} & 0 & M_{q} \end{pmatrix} \begin{pmatrix} x \\ \theta \\ u \\ q \end{pmatrix} + \begin{pmatrix} 0 \\ 0 \\ 0 \\ M_{\mu} \end{pmatrix} \mu_{\text{pitch}} $ |

serial bus (USB) adapter ** shown in Fig. 1. The data logging code was also provided along with the SDI-12 USB adapter to collect sonic anemometer data on the GCS with an update rate of 0.6 Hz.

VI. Results and Discussion

A. System Identification Results

1. Model Structure Determination

After the system identification flight experiments were completed, the input and output measurements were used to characterize the plunge, yaw, roll, and pitch dynamics of the puller and pusher aircraft in hovering flight. The results from this analysis led to the characterization of the plunge, yaw, roll, and pitch models described in Table 1. We also note that the model parameter Z_z was included in our modeling to account for the effects of position control on the closed-loop dynamics of puller and pusher hexacopters. Furthermore, time delays resulting from transmission and computation delays, as well as phase lag due to neglected higher-order dynamics, were not modeled separately; and they can potentially impact the accuracy of puller and pusher hexacopter wind estimates.

^{¶&}lt;sup>64</sup>Atmos22 Ultrasonic Anemometer," M. Environment, https://www.metergroup.com/environment/products/atmos-22-sonic-anemometer/ [retrieved 2020].

^{**&}quot;SDI-12 USB Adapter with Large Terminals," Official Blog (online database), LiuDr Electronic Solutions, Sartell, MN, 31 July 2019, https://liudr.wordpress.com/2019/07/31/sdi-12-usb-adapter-with-larger-terminals-2/[retrieved 2020].

| Table 2 Plunge, yaw, ron, and pitch model parameters identified for puller and pusher nexacopters | | | | | | | | | | |
|---|-------------|---------|----------------|--------------------|-------------------|---------|----------------|--------------------|--|--|
| | | Pulle | er hexacopter | | Pusher hexacopter | | | | | |
| Hexacoptermodel | Parameter | Value | Standard error | Units | Parameter | Value | Standard error | Units | | |
| Plunge | Z_z | -0.13 | 0.0 | $1/s^{2}$ | Z_z | -0.10 | 0.00 | 1/s ² | | |
| | Z_w | -0.18 | 0.02 | 1/kg | Z_w | -0.62 | 0.01 | 1/s | | |
| | Z_{μ} | 21.41 | 0.20 | $1/s^2$ | Z_{μ} | 17.87 | 0.14 | 1/kg | | |
| Yaw | N_{ψ} | -165.70 | 0.69 | $1/s^2$ | N_{ψ} | -131.83 | 0.85 | $1/s^2$ | | |
| | N_r | -23.16 | 0.19 | 1/s | N_r | -11.29 | 0.09 | 1/s | | |
| | N_{μ} | 160.74 | 1.21 | $1/(kg\cdot m^2)$ | N_{μ} | 149.81 | 1.16 | $1/(kg \cdot m^2)$ | | |
| Roll | Y_{ϕ} | 3.70 | 0.51 | m/s^2 | Y_{ϕ} | 1.05 | 0.51 | m/s | | |
| | Y_v | -2.40 | 0.55 | 1/s | Y_v | -13.56 | 0.55 | 1/s | | |
| | Y_p | -2.10 | 0.08 | m/s | Y_p | -2.92 | 0.08 | m/s | | |
| | L_{ϕ} | -371.7 | 1.00 | $1/s^2$ | L_{ϕ} | -247.66 | 1.00 | $1/s^2$ | | |
| | L_p | -8.20 | 0.07 | 1/s | L_p | -8.49 | 0.07 | 1/s | | |
| | L_{μ} | 361.60 | 1.93 | $1/(kg\cdot m^2)$ | L_{μ} | 253.18 | 1.93 | $1/(kg \cdot m^2)$ | | |
| Pitch | $X_{	heta}$ | -2.80 | 0.13 | m/s^2 | $X_{	heta}$ | -4.0 | 0.09 | m/s^2 | | |
| | X_u | -3.60 | 0.12 | 1/s | X_u | -1.0 | 0.03 | 1/s | | |
| | X_q | 2.41 | 0.04 | m/s | X_q | 2.6 | 0.03 | m/s | | |
| | $M_{	heta}$ | -523.81 | 2.13 | $1/s^2$ | $M_{	heta}$ | -274.9 | 1.78 | $1/s^{2}$ | | |
| | M_q | -5.69 | 0.09 | 1/s | M_q | -9.00 | 0.12 | 1/s | | |
| | M_{μ} | 450.21 | 3.33 | $1/(kg \cdot m^2)$ | M_u | 195.5 | 2.51 | $1/(kg \cdot m^2)$ | | |

Table 2 Plunge, vaw, roll, and pitch model parameters identified for puller and pusher hexaconters

2. Model Parameter Estimates

Following the characterization of the plunge, yaw, roll, and pitch model structures for puller and pusher hexacopters, the corresponding parameter values were estimated using the output error parameter estimation method. As shown in Table 2, the parameter values of the plunge, yaw, roll, and pitch models identified for puller and pusher hexacopters were estimated with relatively small standard error values. Moreover, the sign convention of parameter estimates was found to be consistent across the plunge, yaw, roll, and pitch models identified for puller and pusher hexacopters. For all models, a positive

input command resulted in a negative moment. However, the magnitude of the model parameter values (i.e., $Z_{\mu}, N_{\mu}, L_{\mu}$, and M_{μ} for the plunge, yaw, roll, and pitch models) were found to be larger for the puller hexacopter.

3. Model Validation

The plunge, yaw, roll, and pitch models identified for puller and pusher hexacopters were validated using an independent set of input-output observations collected during system identification experiments. As shown in Figs. 2 and 3, the time histories of the

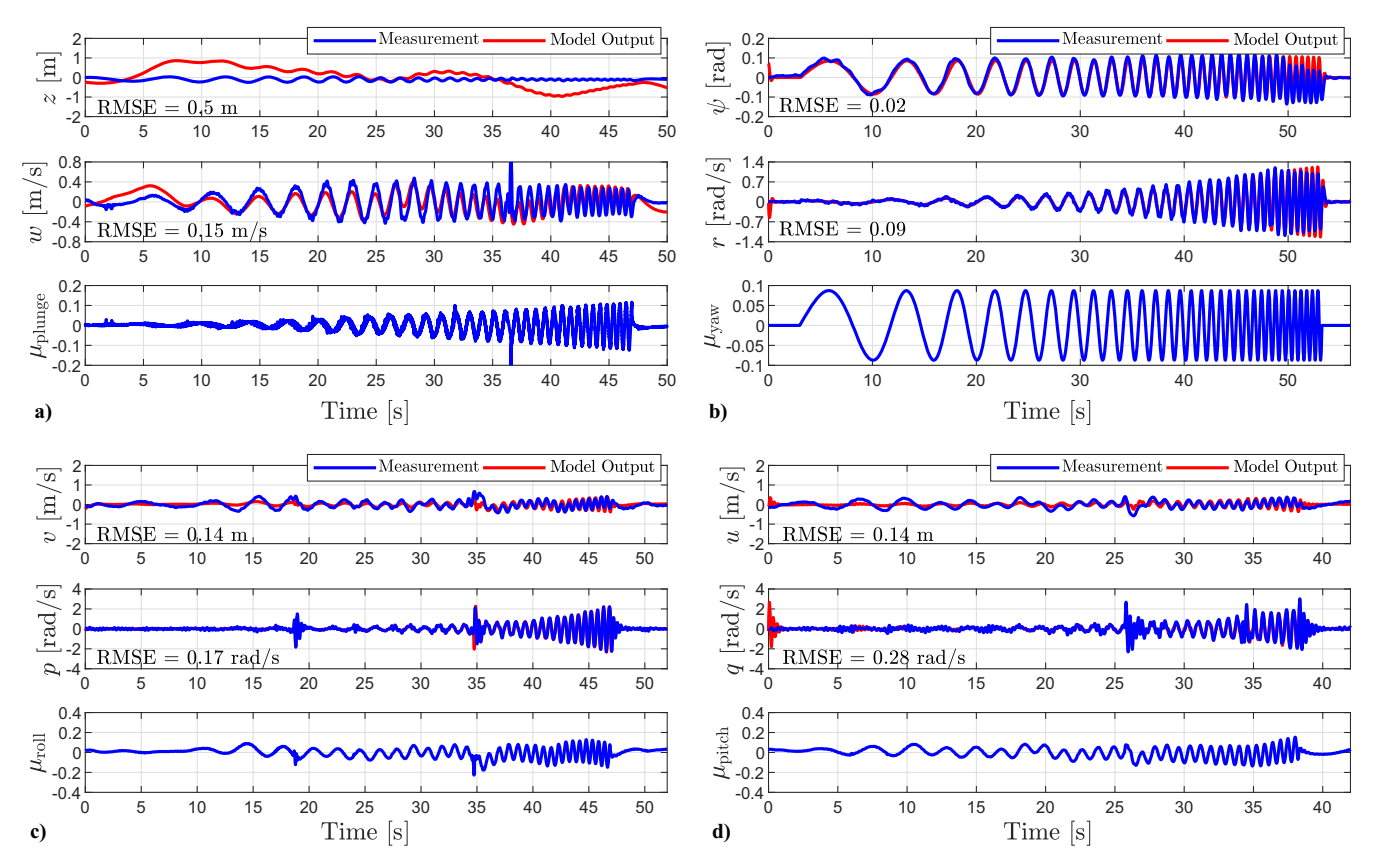


Fig. 2 Validation of the a) plunge, b) yaw, c) roll, and d) pitch models identified for the puller hexacopter.

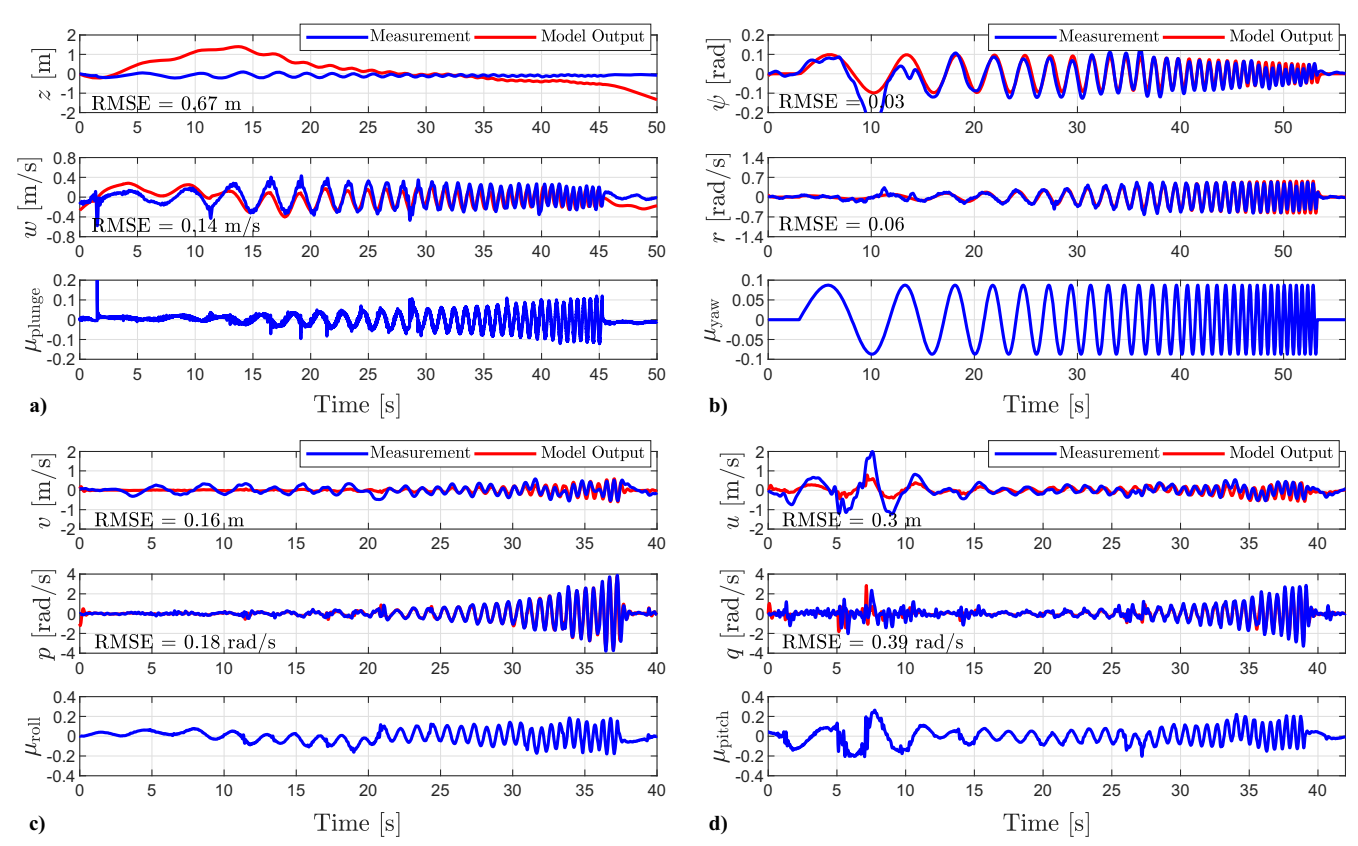


Fig. 3 Validation of the a) plunge, b) yaw, c) roll, and d) pitch models identified for the pusher hexacopter.

puller and pusher hexacopter flight measurements and model outputs were compared. Overall, the performances of the plunge, yaw, roll, and pitch models were found to be comparable across puller and pusher hexacopters based on root-mean-squared error measurements (see Figs. 2 and 3). However, a more significant difference in root-mean-squared values was observed across the pitch models identified for puller and pusher hexacopters. The larger difference in the root-mean-squared error values may be attributed to a brief loss of communication between the motion capture system and the pusher hexacopter 7 s into the flight.

B. Wind Sensing

A total of twelve 3 min flight tests were conducted to evaluate the performance of puller and pusher hexacopters estimating wind velocity while hovering. Atmospheric winds during this period were blowing from the north, with wind speeds varying between calm $(V_{\rm w}\approx 0)$ and 4 m/s (see Figs. 4 and 5).

After the flight tests were completed, the accuracy of the puller and pusher hexacopter wind velocity estimates was evaluated using sonic anemometer observations as reference. Hexacopter and sonic anemometer measurements of $u_{\rm w}$ and $v_{\rm w}$ wind velocity components were compared using mean absolute error (MAE) and root-mean-squared error (RMSE) metrics. The results from this analysis for puller and pusher hexacopters are shown in Tables 3 and 4, respectively. On average, the puller hexacopter estimated $u_{\rm w}$ and $v_{\rm w}$ with MAE values of 0.42 and 0.55 m/s and RMSE values of 0.54 and 0.42 m/s. Similarly, the pusher hexacopter estimated $u_{\rm w}$ and $v_{\rm w}$ with MAE values of 0.69 and 0.37 m/s and RMSE values of 0.48 and 0.58 m/s. Therefore, we found the puller and pusher hexacopters to have a comparable performance measuring the prevailing wind conditions.

A frequency-domain analysis was conducted to determine the performance of the puller and pusher hexacopters resolving time-varying fluctuations of $u_{\rm w}$. First, the power spectral density estimates of the hexacopter and sonic anemometer measurements of $u_{\rm w}$ were compared across the sampled frequency range (0,0.25] Hz. As shown in Fig. 6, the puller and pusher hexacopters can both capture the power distribution of wind fluctuations based on sonic anemometer

measurements. The puller hexacopter was found to underestimate the amplitude of wind fluctuations across most of the sampled frequency range (see Fig. 6c). The pusher hexacopter, on the other hand, was found to consistently overestimate the amplitude of wind fluctuations, but it agreed more consistently with the power spectral density estimates derived from sonic anemometer wind observations (see Fig. 6d). Additionally, a cross-power spectral density analysis was performed to determine the coherence and phase lag between the hexacopter and sonic anemometer measurements of wind fluctuations. As shown in Fig. 7, wind fluctuation estimates from pusher hexacopter were found to have higher coherence and smaller phase lag in comparison with the sonic anemometer observations. Therefore, the findings from this frequency-domain analysis demonstrate that although the puller and pusher hexacopters have similar performances measuring prevailing winds, the pusher hexacopter can measure time-varying wind fluctuations with higher accuracy.

A frequency response analysis was conducted to evaluate the influence that the feedback stabilization of puller and pusher hexacopters has on the fidelity of wind velocity estimates. The transfer functions used in this analysis, $H_{\text{puller}}(s)$ and $H_{\text{pusher}}(s)$, map the input μ_{pitch} to the output θ based on the pitch models identified for puller and pusher hexacopters:

$$H_{\text{puller}}(s) = \frac{558.1s^2 + 2009}{s^3 + 9.3s^2 + 544.3s + 1886} \tag{8}$$

$$H_{\text{pusher}}(s) = \frac{256.1s + 256.1}{s^3 + 10\ s^2 + 256.9s + 247.9} \tag{9}$$

The results from this analysis demonstrate that the -3 dB cutoff frequencies of $H_{\rm puller}(s)$ and $H_{\rm pusher}(s)$ exceed the Nyquist frequency of the sonic anemometer wind velocity observations (0.25 Hz) by margins of 3.41 and 5.35 Hz, respectively (see Fig. 8). Therefore, differences in the feedback-stabilized pitch dynamics of the puller and pusher hexacopters are ruled out as a factor limiting the fidelity of puller and pusher hexacopter wind fluctuation estimates.

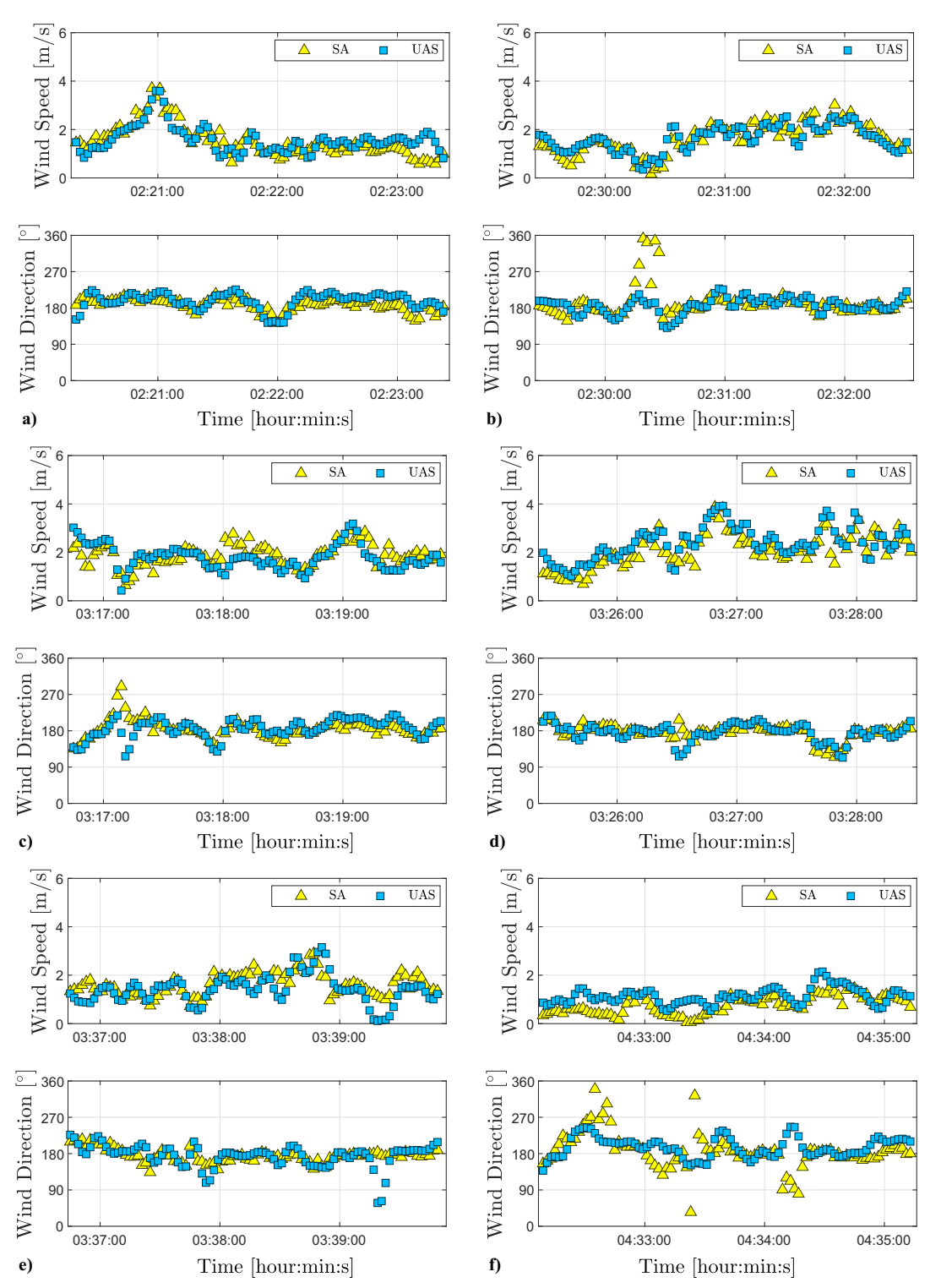


Fig. 4 Comparison of puller hexacopter and sonic anemometer measurements of wind speed and wind direction collected from 1:50 to 4:40 AM Eastern Daylight Time (EDT) on 26 September 2020. UAS denotes unmanned aircraft system (SA, sonic anemometer; UAS, unmanned aircraft system).

VII. Conclusions

System identification experiments were performed to characterize the closed-loop dynamics of puller and pusher hexacopters while hovering in equilibrium flight. Validation results from these experiments demonstrate that the plunge, yaw, roll, and pitch dynamics of puller and pusher hexacopters are well characterized by linear models with identical parametric models (see Figs. 2 and 3). However, consistent differences were observed across the input parameters of the puller and pusher hexacopters. As shown in Table 2, the input parameters identified for the plunge, yaw, roll, and pitch models of the pusher hexacopter were consistently of

lower magnitudes. These results suggest that the pusher hexacopter can track reference input commands exerting less control effort, which can be attributed to the pusher hexacopter having a greater thrust efficiency in hovering flight (see Ref. [18]).

The frequency-domain analysis shows the pusher hexacopter to have a higher performance resolving time-varying wind fluctuations, although the performance of puller and pusher hexacopters estimating general trends in wind velocity was found to be comparable based on the results shown in Tables 3 and 4. As shown in Fig. 6, the power spectral density estimates of the pusher hexacopter and the sonic anemometer measurements of \tilde{u}_w were in closer agreement throughout

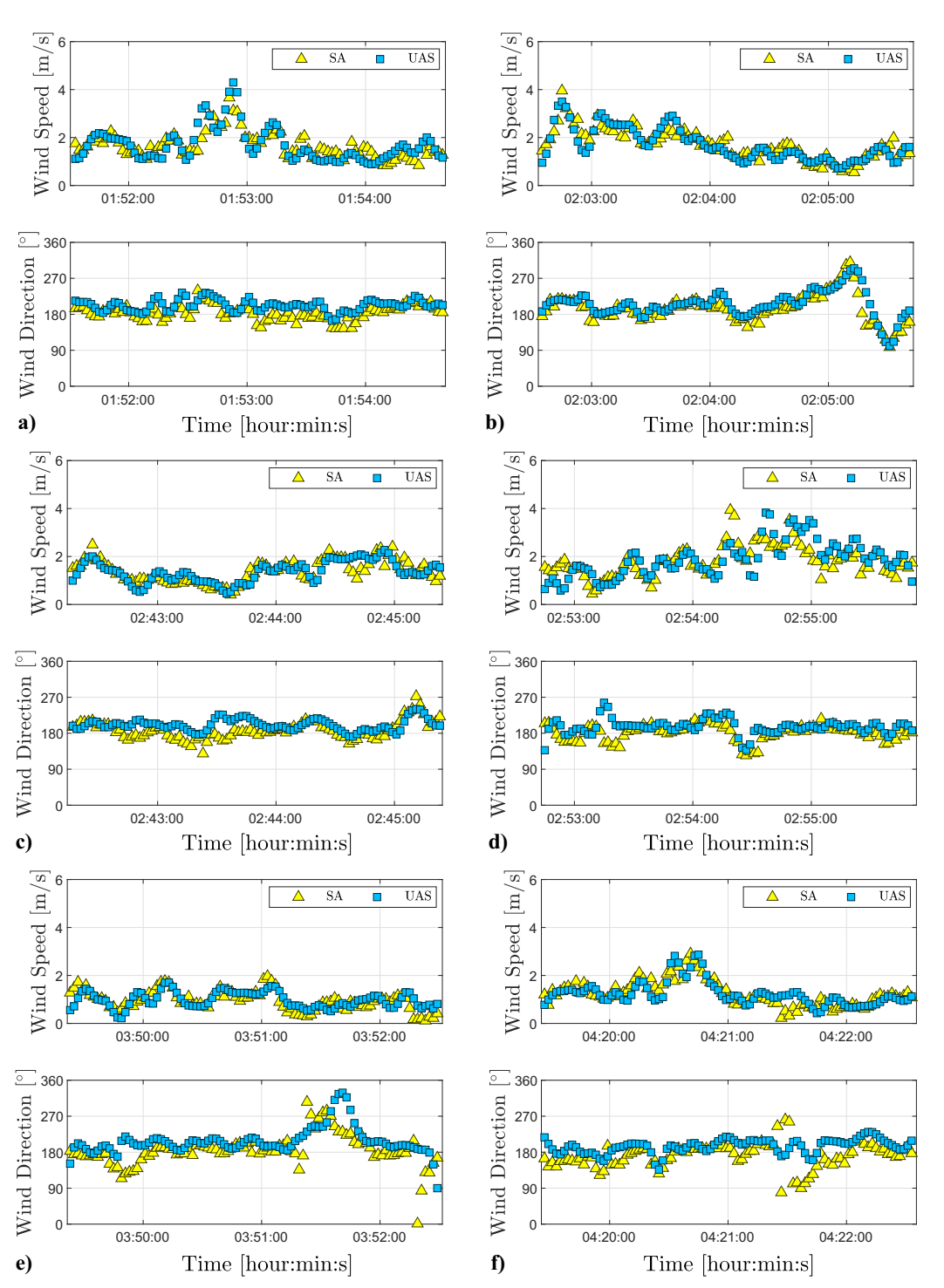


Fig. 5 Comparison of pusher hexacopter and sonic anemometer measurements of wind speed and wind direction collected from 1:50 to 4:30 AM EDT on 25 September 2020.

Table 3 Puller hexacopter MAE, RMSE, and correlation coefficients for $u_{\rm w}$ and $v_{\rm w}$ wind velocity components

| | Sonic anemometer | | Puller hexacopter | | | | | | | |
|----------------|------------------|------------------|-------------------|----------------|------------------------------|------------------------------|---------------------------------------|---|--|--|
| Flight no. | $E(u_{\rm w}^*)$ | $E(v_{\rm w}^*)$ | $E(u_{\rm w})$ | $E(v_{\rm w})$ | $E(u_{\rm w}^*-u_{\rm w})$ | $E(v_{\rm w}^*-v_{\rm w})$ | $\sqrt{E((u_{\rm w}^*-u_{\rm w})^2)}$ | $\sqrt{E((v_{\rm w}^* - v_{\rm w})^2)}$ | | |
| 1 | 0.28 | 1.44 | 0.51 | 1.42 | 0.4 | 0.49 | 0.45 | 0.34 | | |
| 2 | 0.14 | 1.51 | 0.21 | 1.53 | 0.36 | 0.48 | 0.45 | 0.34 | | |
| 3 | 0.08 | 1.76 | 0.21 | 1.64 | 0.48 | 0.63 | 0.65 | 0.51 | | |
| 4 | -0.15 | 1.98 | -0.16 | 2.24 | 0.45 | 0.63 | 0.59 | 0.46 | | |
| 5 | -0.16 | 1.54 | -0.07 | 1.31 | 0.41 | 0.52 | 0.59 | 0.45 | | |
| 6 | 0.02 | 0.65 | 0.27 | 1 | 0.41 | 0.52 | 0.51 | 0.41 | | |
| Average values | | | | | 0.42 | 0.55 | 0.54 | 0.42 | | |

Table 4 Pusher hexacopter MAE, RMSE, and correlation coefficients for $u_{\rm w}$ and $v_{\rm w}$ wind velocity components

| | Sonic anemometer | | Pusher hexacopter | | | | | | |
|----------------|------------------|------------------|-------------------|----------------|--------------------------------|--------------------------------|---------------------------------------|---|--|
| Flight no. | $E(u_{\rm w}^*)$ | $E(v_{\rm w}^*)$ | $E(u_{\rm w})$ | $E(v_{\rm w})$ | $E(u_{\rm w}^* - u_{\rm w})$ | $E(v_{\rm w}^* - v_{\rm w})$ | $\sqrt{E((u_{\rm w}^*-u_{\rm w})^2)}$ | $\sqrt{E((v_{\rm w}^* - v_{\rm w})^2)}$ | |
| 1 | 0.10 | 1.59 | 0.64 | 1.52 | 0.57 | 0.41 | 0.71 | 0.53 | |
| 2 | 0.28 | 1.48 | 0.58 | 1.39 | 0.46 | 0.37 | 0.56 | 0.47 | |
| 3 | 0.20 | 1.27 | 0.66 | 1.29 | 0.51 | 0.29 | 0.59 | 0.38 | |
| 4 | 0.03 | 1.69 | 0.69 | 1.78 | 0.7 | 0.47 | 0.82 | 0.62 | |
| 5 | 0.08 | 0.84 | 0.61 | 0.79 | 0.55 | 0.33 | 0.63 | 0.41 | |
| 6 | -0.15 | 1.13 | 0.45 | 1.17 | 0.71 | 0.35 | 0.8 | 0.46 | |
| Average values | | | | | 0.69 | 0.37 | 0.48 | 0.58 | |

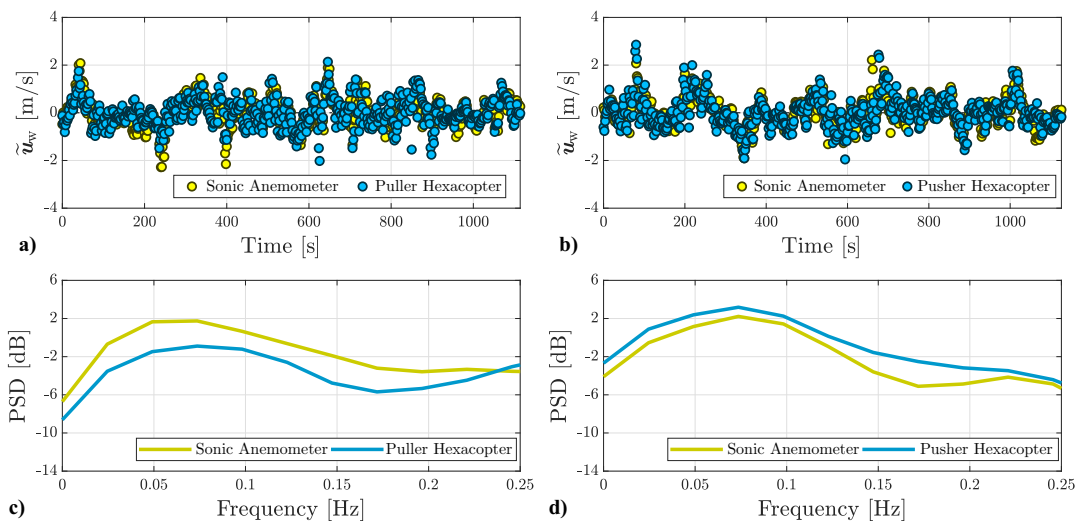


Fig. 6 The zero-mean time-varying fluctuations of \tilde{u}_w estimates from the a) puller and b) pusher hexacopters and the associated power spectral density (PSD) estimates for the c) puller and d) pusher hexacopters.

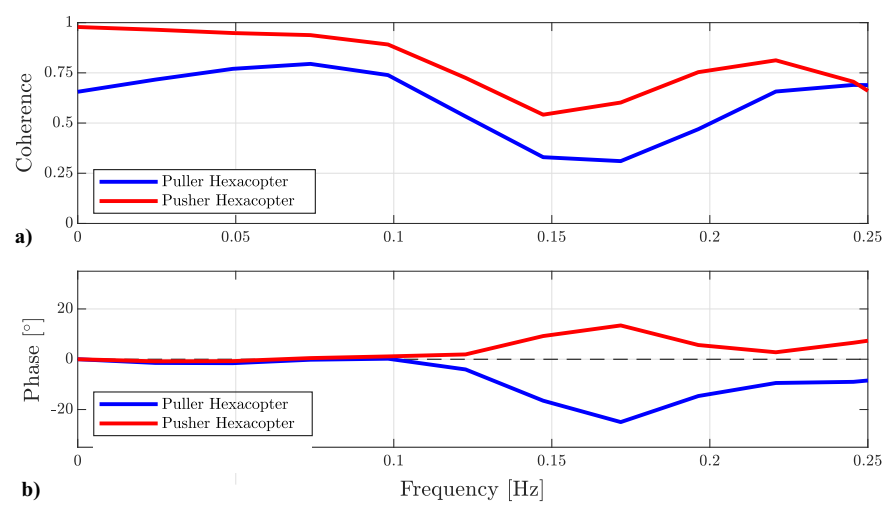


Fig. 7 Coherence and phase lag estimates of puller and pusher hexacopter wind estimates.

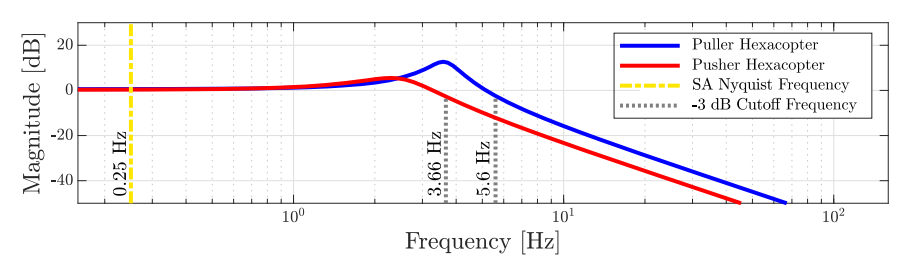


Fig. 8 A comparison of the -3 dB cutoff frequencies of $H_{puller}(s)$ and $H_{pusher}(s)$ and the Nyquist frequency of the sonic anemometer wind observations.

the frequency range of wind fluctuations extending from 0 to 0.25 Hz. The coherence and phase lag evaluation of the hexacopter estimates and sonic anemometer measurements of $\tilde{u}_{\rm w}$ also demonstrated the pusher hexacopter to estimate wind velocity fluctuations with higher accuracy. As shown in Fig. 7, the coherence between pusher hexacopter estimates and sonic anemometer measurements was found to be consistently greater, and the phase lag between pusher hexacopter estimates and sonic anemometer measurements of $\tilde{u}_{\rm w}$ was found to be smaller.

The difference observed across the performances of puller and pusher hexacopters measuring time-varying wind fluctuations is attributed to the pusher hexacopter having an enhanced sensitivity to wind gusts. The higher sensitivity to wind gusts is likely due to the pusher hexacopter having higher drag in air-relative motion, as reported in Ref. [18]. Additionally, findings from a frequency response analysis show that the feedback-stabilization characteristics of puller and pusher hexacopters have an insignificant influence in the estimation of time-varying wind fluctuations. As shown in Fig. 8, the -3 dB frequency cutoff of the puller and pusher hexacopter feedback-stabilized dynamics are well above the Nyquist sampling frequency of the sonic anemometer. The current findings suggest that exploiting the aerodynamic characteristics of pusher hexacopter platforms to estimate wind velocity provides a new opportunity for complementing conventional observations of wind velocity fluctuations in the lower atmosphere.

Acknowledgments

The authors gratefully acknowledge the financial support from the Center for Unmanned Aircraft Systems (UAS), the National Science Foundation (NSF) I/Industry-University Research Partnerships (UCRC) (grant no. CNS-1650465), and NASA (grant no. 80NSSC 20M0162). The authors also gratefully acknowledge the constructive feedback from anonymous reviewers. Additionally, the authors are thankful to David G. Schmale, III, of Virginia Polytechnic Institute and State University's School of Plant and Environmental Sciences, who provided equipment to support the wind estimation validation experiments.

References

- [1] González-Rocha, J., Woolsey, C. A., Sultan, C., de Wekker, S., and Rose, N., "Measuring Atmospheric Winds from Quadrotor Motion," AIAA Atmospheric Flight Mechanics Conference, AIAA Paper 2017-1189, 2017. https://doi.org/10.2514/6.2017-1189
- [2] González-Rocha, J., Woolsey, C. A., Sultan, C., and De Wekker, S. F. J., "Sensing Wind from Quadrotor Motion," *Journal of Guidance, Control, and Dynamics*, Vol. 42, No. 4, 2019, pp. 836–852. https://doi.org/10.2514/1.G003542
- [3] Barbieri, L., Kral, S. T., Bailey, S. C. C., Frazier, A. E., Jacob, J. D., Reuder, J., Brus, D., Chilson, P. B., Crick, C., Detweiler, C., Doddi, A., Elston, J., Foroutan, H., González-Rocha, J., Greene, B. R., Guzman, M. I., Houston, A. L., Islam, A., Kemppinen, O., Lawrence, D., Pillar-Little, E. A., Ross, S. D., Sama, M. P., Schmale, I., David, G., Schuyler, T. J., Shankar, A., Smith, S. W., Waugh, S., Dixon, C., Borenstein, S., and de Boer, G., "Intercomparison of Small Unmanned Aircraft System (sUAS) Measurements for Atmospheric Science During the LAPSE-RATE Campaign," Sensors, Vol. 19, No. 9, 2019, Paper 2179. https://doi.org/10.3390/s19092179
- [4] Pinto, J. O., Jensen, A. A., Steiner, M., O'Sullivan, D., Taylor, S., Elston, J., Baker, C. B., Hotz, D., Marshall, C., Jacob, J., Barfuss, K., Piguet, B., and Roberts, G., "The Status and Future of Small Uncrewed Aircraft Systems (UAS) in Operational Meteorology," *Bulletin of the American Meteorological Society*, Vol. 102, No. 11, 2021, pp. E2121–E2139. https://doi.org/10.1175/BAMS-D-20-0138.1
- [5] González-Rocha, J., Sosa, A. J., Hanlon, R., Allen, A. A., Rypina, I., Schmale, D. G., III, and Ross, S. D., "Multirotor-Assisted Measurements of Wind-Induced Drift of Irregularly Shaped Objects in Aquatic Environments," *Applied Ocean Research*, Vol. 110, May 2021, Paper 102538. https://doi.org/10.1016/j.apor.2021.102538
- [6] Steiner, M., "Urban Air Mobility: Opportunities for the Weather Community," *Bulletin of the American Meteorological Society*, Vol. 100, No. 11, 2019, pp. 2131–2133. https://doi.org/10.1175/BAMS-D-19-0148.1
- [7] Stith, J. L., Baumgardner, D., Haggerty, J., Hardesty, R. M., Lee, W.-C., Lenschow, D., Pilewskie, P., Smith, P. L., Steiner, M., and Vömel, H., "100 Years of Progress in Atmospheric Observing

- Systems," *Meteorological Monographs*, Vol. 59, Jan. 2018, pp. 2.1–2.55. https://doi.org/10.1175/AMSMONOGRAPHS-D-18-0006.1
- [8] Haupt, S. E., Rauber, R. M., Carmichael, B., Knievel, J. C., and Cogan, J. L., "100 Years of Progress in Applied Meteorology. Part I: Basic Applications," *Meteorological Monographs*, Vol. 59, Jan. 2018, pp. 22.1–22.33. https://doi.org/10.1175/AMSMONOGRAPHS-D-18-0004.1
- [9] Muñoz-Esparza, D., Sharman, R., Sauer, J., and Kosović, B., "Toward Low-Level Turbulence Forecasting at Eddy-Resolving Scales," *Geo-physical Research Letters*, Vol. 45, No. 16, 2018, pp. 8655–8664. https://doi.org/10.1029/2018GL078642
- [10] Nolan, P. J., Pinto, J., González-Rocha, J., Jensen, A., Vezzi, C., Bailey, S., de Boer, G., Diehl, C., Laurence, R., Powers, C., Ross, S. D., and Schmale, D. G., III, "Coordinated Unmanned Aircraft System (UAS) and Ground-Based Weather Measurements to Predict Lagrangian Coherent Structures (LCSs)," Sensors, Vol. 18, No. 12, 2018, Paper 4448. https://doi.org/10.3390/s18124448
- [11] Nolan, P. J., McClelland, H. G., Woolsey, C. A., and Ross, S. D., "A Method for Detecting Atmospheric Lagrangian Coherent Structures Using a Single Fixed-Wind Unmanned Aircraft System," *Sensors*, Vol. 19, No. 7, 2019, Paper 1607. https://doi.org/10.3390/s19071607
- [12] Hanlon, R., Jacquemin, J. J., Birbeck, J. A., Westrick, J. A., Harb, C., Gruszewski, H., Ault, A. P., Durelle, S., Housein, F., Ross, S. D., González-Rocha, J., Powers, C., Pratt, L., Looney, H., Baker, G., and Schmale, D. G., III, "Drone-Based Water Sampling and Characterization of Three Freshwater Harmful Algal Blooms in the United States," Frontiers in Remote Sensing, Vol. 3, Aug. 2022, Paper 949052. https://doi.org/10.3389/frsen.2022.949052
- [13] Andersen, T., Scheeren, B., Peters, W., and Chen, H., "A UAV-Based Active AirCore System for Measurements of Greenhouse Gases," *Atmospheric Measurement Techniques*, Vol. 11, No. 5, 2018, pp. 2683–2699. https://doi.org/10.5194/amt-11-2683-2018
- [14] Morales, R., Ravelid, J., Vinkovic, K., Korbeń, P., Tuzson, B., Emmenegger, L., Chen, H., Schmidt, M., Humbel, S., and Brunner, D., "Controlled-Release Experiment to Investigate Uncertainties in UAV-Based Emission Quantification for Methane Point Sources," Atmospheric Measurement Techniques, Vol. 15, April 2022, pp. 2177–2198. https://doi.org/10.5194/amt-15-2177-2022
- [15] Palomaki, R. T., Rose, N. T., van den Bossche, M., Sherman, T. J., and De Wekker, S. F., "Wind Estimation in the Lower Atmosphere Using Multirotor Aircraft," *Journal of Atmospheric and Oceanic Technology*, Vol. 34, No. 5, 2017, pp. 1183–1191. https://doi.org/10.1175/JTECH-D-16-0177.1
- [16] González-Rocha, J., De Wekker, S. F., Ross, S. D., and Woolsey, C. A., "Wind Profiling in the Lower Atmosphere from Wind-Induced Perturbations to Multirotor UAS," *Sensors*, Vol. 20, No. 5, 2020, Paper 1341. https://doi.org/10.3390/s20051341
- [17] Bilyeu, L., Bloomfield, B., Hanlon, R., González-Rocha, J., Jacquemin, S. J., Ault, A. P., Birbeck, J. A., Westrick, J. A., Foroutan, H., Ross, S. D., and Schmale, D. G., III, "Drone-Based Particle Monitoring Above Two Harmful Algal Blooms (HABs) in the USA," *Environmental Science: Atmospheres*, Vol. 2, No. 6, 2022, pp. 1351–1363. https://doi.org/10.1039/d2ea00055e
- [18] Sharma, P., and Atkins, E., "Experimental Investigation of Tractor and Pusher Hexacopter Performance," *Journal of Aircraft*, Vol. 56, No. 5, 2019, pp. 1920–1934. https://doi.org/10.2514/1.C035319
- [19] Cunningham, M., and Hubbard, J. E., "Open Loop System Identification of a Small Multirotor Vehicle with an Active Feedback Control System," *Atmospheric Flight Mechanics Conference*, AIAA Paper 2018-3475, 2018. https://doi.org/10.2514/6.2018-3475
- [20] Gandhi, M. S., Whitcher, L., Theodorou, E., and Johnson, E. N., "Practical System Identification for Small VTOL Unmanned Aerial Vehicle," AIAA SciTech Forum, AIAA Paper 2019-1982, 2019. https://doi.org/10.2514/6.2019-1982
- [21] Berger, T., Lopez, M. J., Wagner, A. M., and Tischler, M. B., "Guidelines for System Identification of Multirotor Vehicles with Highly Correlated Inputs," *Vertical Flight Society's 76th Annual Forum and Technology Display*, The Vertical Flight Soc., Fairfax, VA, 2020, pp. 1–17.
- [22] Berger, T., and Lopez, M. J. S., "Frequency Domain Identification of a Multi-Input Control Equivalent Turbulence Input Model," *Journal of Guidance, Control, and Dynamics*, Vol. 45, No. 1, 2022, pp. 15–27. https://doi.org/10.2514/1.G006044
- [23] Klein, V., and Morelli, E. A., Aircraft System Identification: Theory and Practice, AIAA, Reston, VA, 2006.
- [24] M-Air (online database), Univ. of Michigan, Ann Arbor, MI, https:// robotics.umich.edu/about/mair/ [retrieved 2020].